Journal of *Marine Science and Engineering*

MDPI

Article

Hydrogen Production Power Supply with Low Current Ripple Based on Virtual Impedance Technology Suitable for Offshore Wind–Solar–Storage System

Peng Chen [1,2], Jiajin Zou [1], Chunjie Wang [1,2,*], Qiang Fu [1,2,3,*], Lin Cui [4] and Lishan Ma [5]

[1] School of Electrical Engineering and Automation, Tianjin University of Technology, Tianjin 300384, China; chenpeng@email.tjut.edu.cn (P.C.); jerryzou@tjut.edu.cn (J.Z.)
[2] Tianjin Key Laboratory of New Energy Power Conversion, Transmission and Intelligent Control, Tianjin University of Technology, Tianjin 300384, China
[3] Haihe Laboratory of Information Technology Application Innovation, Tianjin 300450, China
[4] Yangtze Delta Marine Technology Innovation Center, Nantong 226100, China; cuilin@mtic-js.cn
[5] National Ocean Technology Center, Ministry of Natural Resources, Tianjin 300112, China; malishan2008@126.com
* Correspondence: chunjie_wang@tjut.edu.cn (C.W.); fuqiang@email.tjut.edu.cn (Q.F.)

Abstract

Hydrogen production from water electrolysis can not only reduce greenhouse gas emissions, but also has abundant raw materials, which is one of the ideal ways to produce hydrogen from new energy. The hydrogen production power supply is the core component of the new energy electrolytic water hydrogen production device, and its characteristics have a significant impact on the efficiency and purity of hydrogen production and the service life of the electrolytic cell. In essence, the DC/DC converter provides the large current required for hydrogen production. For the converter, its input still needs the support of a DC power supply. Given the maturity and technical characteristics of new energy power generation, integrating energy storage into offshore energy systems enables stable power supply. This configuration not only mitigates energy fluctuations from renewable sources but also further reduces electrolysis costs, providing a feasible pathway for large-scale commercialization of green hydrogen production. First, this paper performs a simulation analysis on the wind–solar hybrid energy storage power generation system to demonstrate that the wind–solar–storage system can provide stable power support. It places particular emphasis on the significance of hydrogen production power supply design—this focus stems primarily from the fact that electrolyzers impose specific requirements on high operating current levels and low current ripple, which exert a direct impact on the electrolyzer's service life, hydrogen production efficiency, and operational safety. To suppress the current ripple induced by high switching frequency and high output current, traditional approaches typically involve increasing the output inductor. However, this method substantially increases the volume and weight of the device, reduces the rate of current change, and ultimately results in a degradation of the system's dynamic response performance. To this end, this paper focuses on developing a virtual impedance control technology, aiming to reduce the ripple amplitude while avoiding an increase in the filter inductor. Owing to constraints in current experimental conditions, this research temporarily relies on simulation data. Specifically, a programmable power supply is employed to simulate the voltage output of the wind–solar–storage hybrid system, thereby bringing the simulation as close as possible to the actual operating conditions of the wind–solar–storage hydrogen production system. The experimental results demonstrate that the proposed method can effectively suppress the ripple amplitude, maintain high operating efficiency, and ultimately meet the expected research objectives. That makes it particularly suitable

check for updates

Academic Editor: Barbara Zanuttigh

Received: 6 September 2025
Revised: 12 October 2025
Accepted: 13 October 2025
Published: 17 October 2025

Citation: Chen, P.; Zou, J.; Wang, C.; Fu, Q.; Cui, L.; Ma, L. Hydrogen Production Power Supply with Low Current Ripple Based on Virtual Impedance Technology Suitable for Offshore Wind–Solar–Storage System. *J. Mar. Sci. Eng.* **2025**, *13*, 1997. https://doi.org/10.3390/jmse13101997

Copyright: © 2025 by the authors. Licensee MDPI, Basel, Switzerland. This article is an open access article distributed under the terms and conditions of the Creative Commons Attribution (CC BY) license (https://creativecommons.org/licenses/by/4.0/).

as a high-quality power supply for offshore hydrogen production systems that have strict requirements on volume and weight.

Keywords: small-signal analysis; virtual impedance; ripple; hydrogen production power supply; comprehensive utilization system of offshore energy

1. Introduction

As a kind of clean and pollution-free secondary energy with high energy density and high conversion efficiency, hydrogen energy is widely used in aerospace, electric power, transportation, chemical industry, metallurgy, and other fields. The most popular way to produce hydrogen is through fossil fuels, which are the least expensive but pollute the environment with carbon dioxide. With the aggravation of the greenhouse effect, green hydrogen production has become a research hotspot. The technology of hydrogen production by electrolysis of water is one of the ideal ways to produce hydrogen because of its simple and easy access to raw materials. However, the cost of hydrogen per standard cubic meter is at least twice the cost of fossil fuel production, and the cost of electricity accounts for about 60–80% of the total hydrogen production cost [1]. Also, the source of electricity is often power plants, indirectly causing carbon dioxide emissions [2]. In addition to traditional energy power generation, new energy power generation technology has become relatively mature, and the cost of electricity is cheaper than traditional energy, which is an ideal power supply for low-cost electrolytic hydrogen production [3,4]. However, the new energy generation has the characteristics of intermittency, volatility, and randomness, which leads to a low energy utilization rate [5]. In order to ensure the stable operation of the system, the energy storage needs to be increased [6]. New energy hydrogen production can not only realize the field development and consumption of volatile new energy, improve energy efficiency, but also realize low-cost and all-green hydrogen production, fundamentally changing the structure of hydrogen production [7]. Hydrogen power supplies need to adapt to the characteristics of the electrolyzer, namely large output current, small output current ripple, high step-down ratio, and wide output voltage range.

Garrigos A. et al. noted that push–pull DC-DC converters are unsuitable for high-power hydrogen production applications due to excessive voltage stress on switching devices [8]. Xin C.N. et al. addressed this issue by proposing a two-stage buck DC-DC converter with a flying-capacitor multilevel topology, which achieves high efficiency and low ripple while matching the electrolyzer's volume requirements [9]. However, this topology requires complex capacitor voltage balancing control. Concha D. et al. developed a DCX two-stage DC-DC converter, but its reliance on a constant current source leads to large output current ripples [10]. Lajos Torok et al. designed a three-phase grid-connected power supply for household electrolyzers, which exhibits high efficiency but fails to meet the high-current demands of industrial-scale hydrogen production [11]. In this paper, according to the characteristics of low voltage and high current output of electrolysis, and the high demand for output current ripple, a design of a phase-shifted full-bridge modular DC high-current hydrogen generation power supply based on virtual impedance technology is proposed. After DC-DC conversion by a phase-shifted full-bridge circuit, it is processed by a subsequent high-frequency transformer, and finally output to the load by a filter circuit. Considering that the device designed in this paper adopts a modular structure with parallel input and parallel output, ripple is a problem that cannot be ignored, especially when the current changes; it is easy to have the superposition of ripples, which makes the current waveform worse. To address these challenges, this study aims to minimize the output

current ripple of the hydrogen production power supply while using a compact output filter inductance. Specifically, we focus on virtual impedance technology int the control to optimize the system's dynamic performance and reduce current ripple amplitude, thereby meeting the high-current and low-ripple requirements of industrial electrolyzers [12–16]. For the limitations of the experimental equipment, a programmable power supply is temporarily utilized to replicate the voltage output of the wind–solar–storage system based on simulation data. This approach is specifically designed to approximate the real working conditions of the wind–solar–storage hydrogen production system to the greatest feasible extent. Based on this, experimental validation was carried out, and the results demonstrated a significant ripple suppression effect. This makes it particularly suitable for offshore hydrogen production systems with high requirements for volume and weight.

2. Simulation Analysis of Wind, Solar, and Storage Power Generation System

The key modules were first modeled to study the system characteristics.

2.1. Simulation Analysis of Offshore Wind–Solar–Storage–Power Generation System

The principal structure of the offshore wind–solar hybrid power generation system is shown in Figure 1.

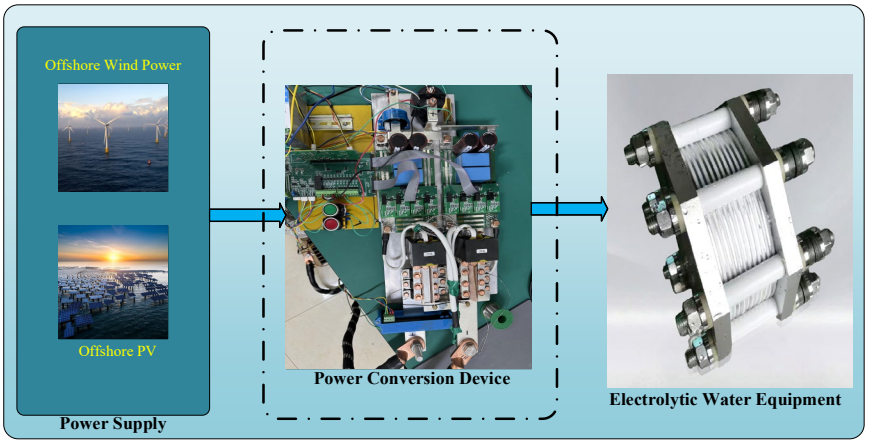

Figure 1. Wind, solar, storage, power generation, and hydrogen production system diagram.

As shown in Figure 1, wind and solar energy are collected and converted into electric energy for hydrogen supply by wind turbines and photovoltaic cells, and the collected electric energy is converted into an electrolytic cell for power supply by hydrogen production power. Although there are many types of hydrogen power sources, they all need to adapt to the characteristics of the electrolyzer; that is, they have the characteristics of large output current, small output current ripple, high step-down ratio, and wide output voltage range.

2.2. Modeling of Wind Turbines and Wind Power Generation Systems

Wind power generation is a process in which wind energy is first converted into mechanical energy, and then mechanical energy is converted into electrical energy. The wind power generation system mainly includes the following parts: wind wheel (converts wind energy into mechanical energy), transmission device (transmits mechanical energy to generator), speed regulation structure (makes the generator run smoothly), generator (converts mechanical energy into electrical energy), tower (supports the unit), yaw system (makes wind energy blow vertically to the wind wheel) and speed limiting structure, etc.

According to the aerodynamic principle of wind power generation, its output power is given by Equation (1) [15].

$$P_W = \frac{1}{2}R^2\rho\pi\lambda C_p(\lambda,\beta)v^3 \tag{1}$$

where, in Equation (1), ρ is density in the air, v is undisturbed wind speed, R is radius of the blades of the wind turbine, λ is blade tip velocity ratio, that is, the ratio of the linear velocity of the blade tip to the wind speed, β is pitch angle, and C_p is wind energy utilization coefficient (generator output power/wind turbine input power).

The wind energy utilization coefficient $C_p(\lambda, \beta)$ is expressed in Equation (2).

$$\begin{cases} C_p(\lambda,\ \beta) = 0.5176(\frac{116}{\lambda_t} - 0.4\beta - 5)^{-\frac{21}{\lambda_t}} + 0.0068\lambda \\ \frac{1}{\lambda_t} = \frac{1}{\lambda+0.08\beta} - \frac{0.035}{\beta^3+1} \end{cases} \tag{2}$$

The tip velocity ratio λ is the ratio of the linear velocity of the blade tip to the wind speed and is calculated in Equation (3).

$$\lambda = \frac{\omega R}{v} = \frac{R\pi n}{30v} \tag{3}$$

where ω is the angular velocity of the rotor rotation, and n is the speed of the wind turbine.

According to the above Equations (1)–(3), the fan model is established, as shown in Figure 2.

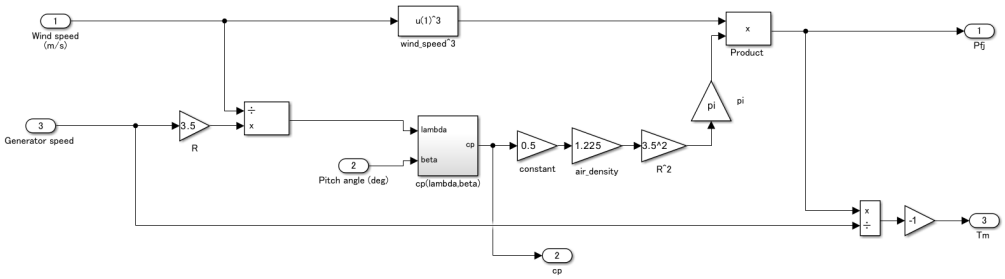

Figure 2. Schematic diagram of the wind turbine model.

The wind turbine main parameters are as follows: rated power is 6 kW, rotor diameter is 7.5 m, three blades, horizontal axis, cut-in wind speed is less than 3.5 m/s, and rated wind speed is 18 m/s.

The wind turbine is equipped with a permanent magnet synchronous generator (PMSG). Fluctuations in wind speed cause variations in the generator's rotational speed, output frequency, and voltage amplitude. To ensure a stable input for the subsequent hydrogen production power supply, the AC output of the PMSG is first converted to DC via a rectifier circuit, and then regulated to a 600 V DC bus voltage through a DC/DC converter. The model settings can be found in Figure 3.

2.3. Modeling of Photovoltaic Power Generation Systems

Solar cells are semiconductor devices that directly convert solar energy into electrical energy, and their basic principle is the "photogenerated voltage effect". Structurally, a solar cell can be seen as a planar, large-area P-N junction with a negative charge in the P region and a positive charge in the N region. When sunlight shines on the P-N junction, conductive photogenerated carriers will be generated on the P-N junction, resulting in holes and electron pairs, and under the action of the electrostatic field, the carriers are separated, the photogenerated holes are in the P region, and the photogenerated electrons

are in the N region, so that the potential in the P region increases, and the potential in the N region decreases, to generate electromotive force on the P-N junction, which is a photovoltaic cell.

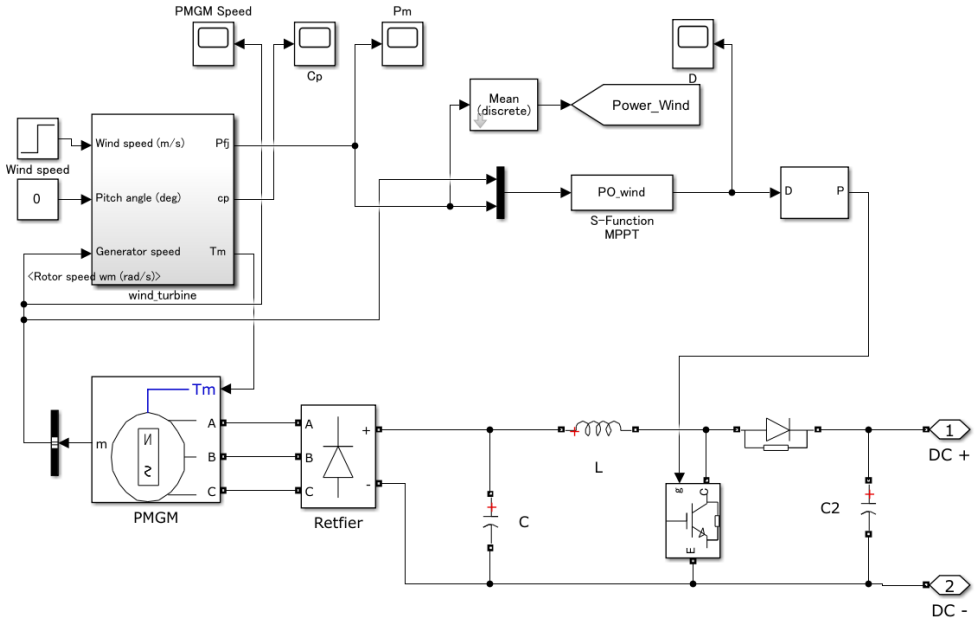

Figure 3. Wind power generation system model.

Figure 4 shows the equivalent circuit diagram of photovoltaic cells.

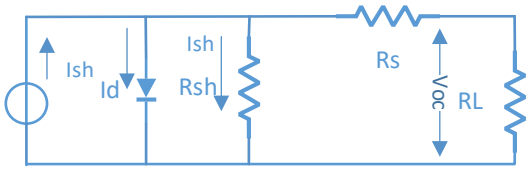

Figure 4. Equivalent circuit diagram of the photovoltaic cell.

The photogenerated current generated by the photovoltaic cell under sunlight is represented by the constant current source I_{sc}, the total diffusion current of the P-N junction is I_d (expressed by the forward current of the diode), and the two flow directions of the photogenerated current and the diffusion current are opposite, and the expression is given in Equation (4) [16].

$$I_d = I_{os}[e^{\frac{qV}{AKT}} - 1] \tag{4}$$

where I_{os} is the diode reverse saturation current in A, q is the electron charge, unit: $1.6021892 \times 10^{-19}$ C; C is the photovoltaic cell output voltage, unit: V, and A is the ideal quality factor. K is the Boltzmann constant, k = $1.3806505 \times 10^{-23}$ J/K, and T is the thermodynamic temperature (surface temperature) of the photovoltaic cell, in K.

According to Equation (4) and Figure 4, the photogenerated current can be obtained as Equation (5).

$$I = I_{sc} - I_0[e^{\frac{q(V+IR_s)}{AKT}} - 1] - \frac{V + IR_s}{R_{sh}} \tag{5}$$

where R_s, R_{sh} are series resistance, parallel resistance, and the unit is Ω. In the circuit analysis calculation, the series resistance R_s is ignored, and the electrical equation of the ideal photovoltaic cell is simplified as Equation (6).

$$I = I_{sc} - I_{os}[e^{\frac{qV}{AKT}} - 1] \tag{6}$$

So

$$V = \frac{1}{q}AKT\ln(\frac{I_{sc} - I}{I_{os}} + 1) \tag{7}$$

According to Equation (6), when the external circuit is 0 (i.e., R_L = 0), the output current of the photovoltaic cell is equal to the photogenerated current I_{sc}, and in the same way, according to Equation (7), when the external circuit is ∞, the open-circuit voltage V_{oc} of the photovoltaic cell can be calculated.

$$V_{oc} = \frac{1}{q}AKT\ln(\frac{I_{sc}}{I_{os}} + 1) \tag{8}$$

According to the established photovoltaic cell model, according to the maximum output voltage of the photovoltaic cell, this paper selects the boost circuit (boost chopper circuit) as the DC/DC conversion circuit, which is mainly composed of the following parts: diode D, filter inductor L, switch Q, and filter capacitor C, and the photovoltaic power generation is boosted to the collection voltage, and the photovoltaic simulation system is shown in Figure 5.

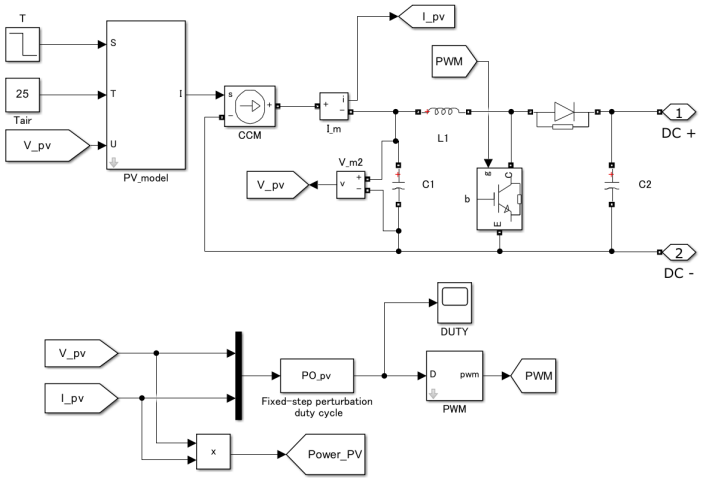

Figure 5. Photovoltaic power generation system model.

2.4. Energy Storage System Model

Wind power generation and photovoltaic power generation systems are unstable. To maintain the stability of the system and provide a stable output for hydrogen production power supply, the system is equipped with a lithium-ion battery system (400 V, 3000 Ah), which is connected to the DC bus through the DC/DC converter.

The model uses Equations (9) and (10) for the lithium-ion battery type [16].

Discharge model:

$$f_1(it, i^*, i) = E_0 - K\frac{Q}{Q - it}i^* - K\frac{Q}{Q - it}it + A \cdot e^{(-B \cdot it)} \tag{9}$$

Charging model:

$$f_2(it, i^*, i) = E_0 - K\frac{Q}{0.1 \cdot Q + it}i^* - K\frac{Q}{Q - it}it + A \cdot e^{(-B \cdot it)} \quad (10)$$

where E_0 is the constant voltage, in V, K is the polarization constant, in V/Ah, or polarization resistance, in Ω, i^* is the low-frequency current dynamics, in A, i is the battery current, in A, it is the extracted capacity, in Ah, Q is the maximum battery capacity, in Ah, A is the exponential voltage, in V, and B is the exponential capacity, in Ah^{-1}.

The model of the energy storage charging and discharging system is constructed as shown in Figure 6.

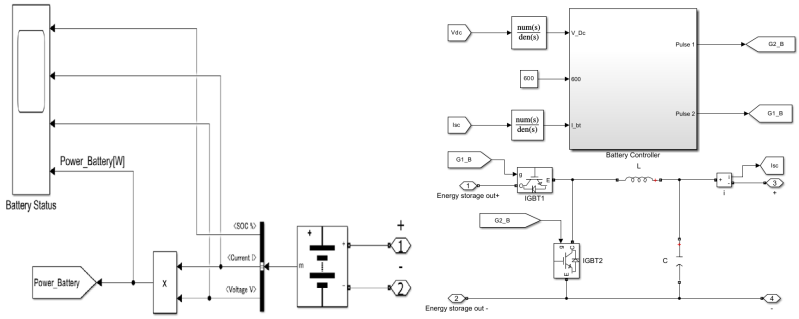

Figure 6. Energy storage battery system. (**a**) Energy storage batteries; (**b**) battery control systems.

2.5. Wind and Solar Storage and Power Generation System Model

The above models are integrated to form a wind–solar–storage–power generation system model, with the load as the resistance, as shown in Figure 7.

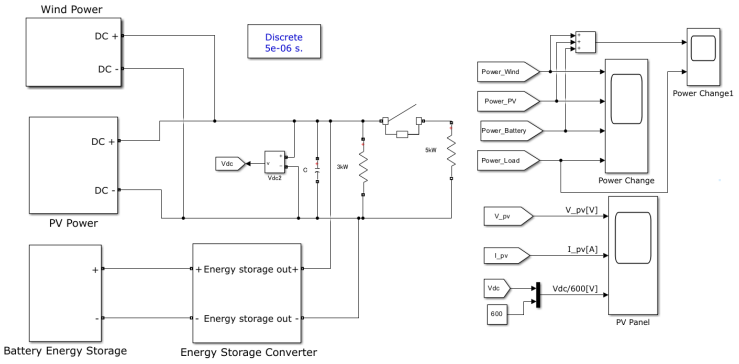

Figure 7. Simulation diagram of wind, solar, storage, and power generation system.

The system simulation is conducted under the following dynamic conditions to evaluate its response to renewable energy fluctuations and load changes: (1) at t = 1 s, the wind speed of the permanent magnet wind turbine is abruptly increased from 6 m/s to 7 m/s; (2) at t = 2 s, the light intensity for photovoltaic power generation is reduced from 1200 W/m^2 to 1000 W/m^2; and (3) at t = 3 s, the load power is suddenly increased from 3 kW to 8 kW.

The simulation results are as follows:

The simulation results are shown in Figures 8–10; that t = 1 s, the wind speed of the permanent magnet wind turbine mutates from 6 m/s to 7 m/s, and the generator speed changes with the wind speed, and the maximum wind energy utilization coefficient Cp wind turbine output power is 3.8 kW when the output power is 6 m/s and output power is 5.6 kW at 7 m/s, which performs well under different wind speeds.

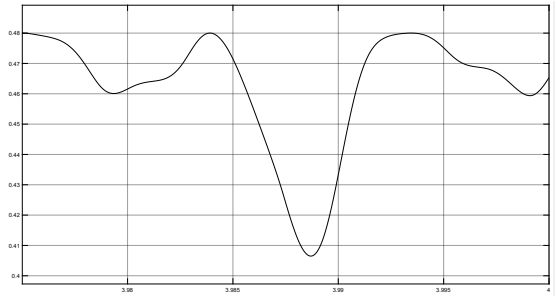

Figure 8. Wind energy utilization coefficient *Cp* varies with wind speed.

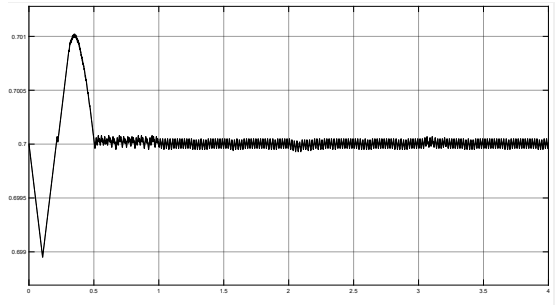

Figure 9. Controller duty under a wind turbine, with maximum wind energy tracking.

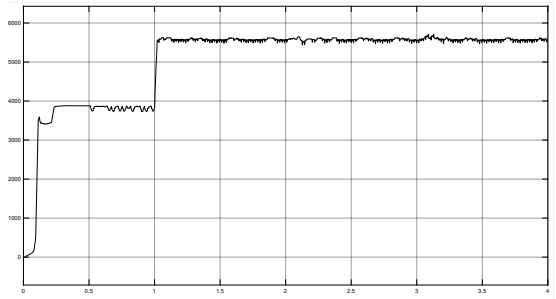

Figure 10. PMSG output power.

The photovoltaic power generation simulation results are shown in Figures 11–14.

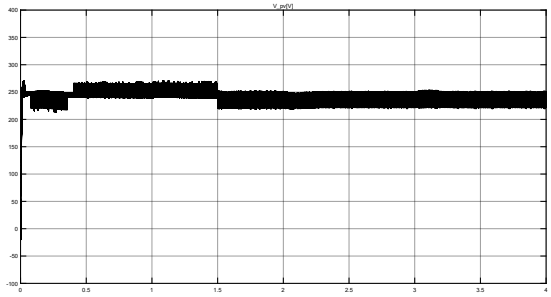

Figure 11. Photovoltaic power generation output voltage.

The simulation results of the photovoltaic power generation system are shown in Figures 11–14 when the light intensity is 1200 W/m^2, the output power of photovoltaic power generation is about 3.7 kW when the light intensity becomes 1000 W/m^2, the output power of photovoltaic power generation is reduced to 3 kW, the output voltage is constant in the process of change, the output current is reduced accordingly, and the response is rapid.

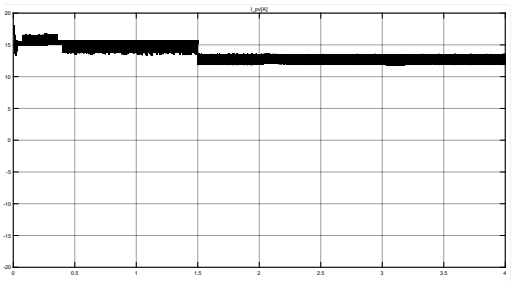

Figure 12. Photovoltaic power generation output current.

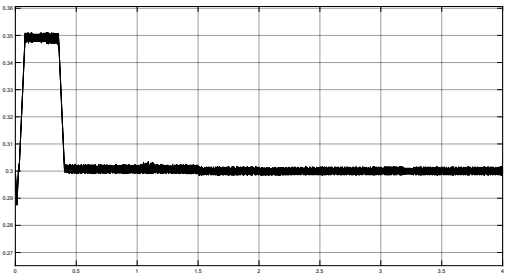

Figure 13. DC converter duty of the photovoltaic system.

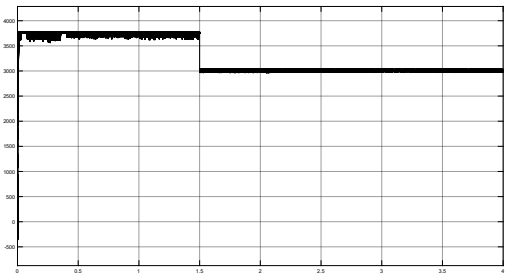

Figure 14. Photovoltaic power output.

To maintain the stability of the system and provide a stable output for the hydrogen production power supply, the system is equipped with a lithium battery system (3000 Ah, 400 V), and the simulation results of the energy storage battery are shown.

The simulation results of the energy storage battery are shown in Figures 15–18, and the battery performs well in the process of charging and discharging, which can effectively balance wind power generation, photovoltaic power generation, and load demand. From the perspective of the changing trend of SOC, the basic battery is shallow charging and shallow discharge, and there is no overcharge or over-discharge. The system exhibits a fast response when the output of wind power generation, photovoltaic power generation, or the load demand changes, and can adjust the charge and discharge in time. There is no obvious fluctuation in the process of charging and discharging, indicating that the system is stable.

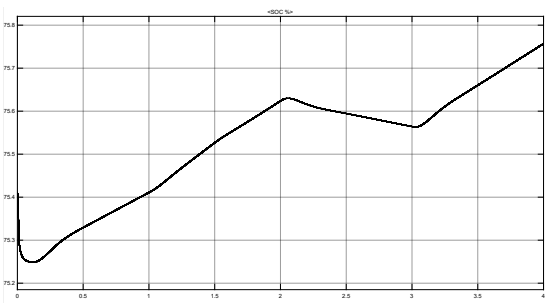

Figure 15. Energy storage battery system SOC.

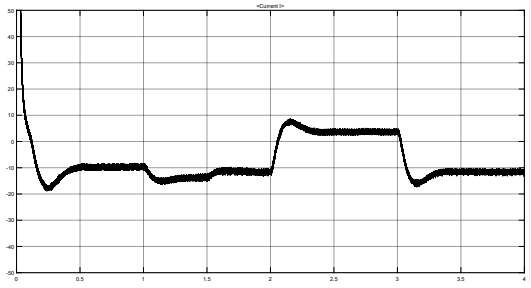

Figure 16. Energy storage battery system current.

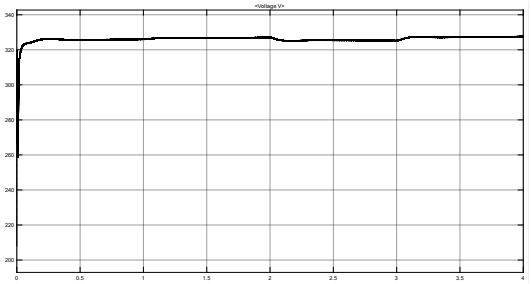

Figure 17. Energy storage battery system output voltage.

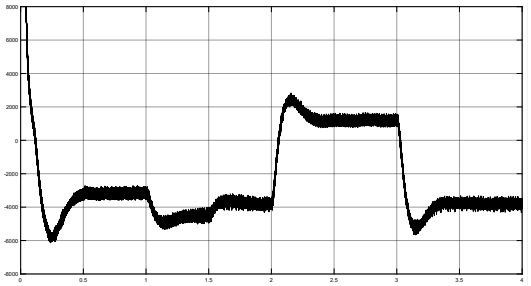

Figure 18. Energy storage battery output power.

Simulations of wind, solar, and storage power generation systems are shown in Figures 19–21.

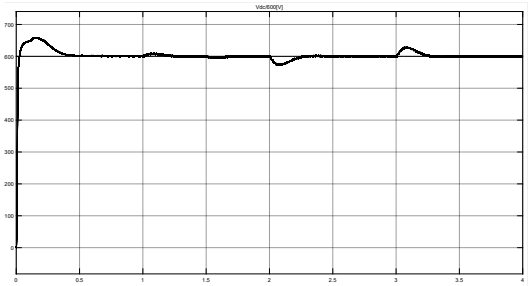

Figure 19. The DC bus voltage.

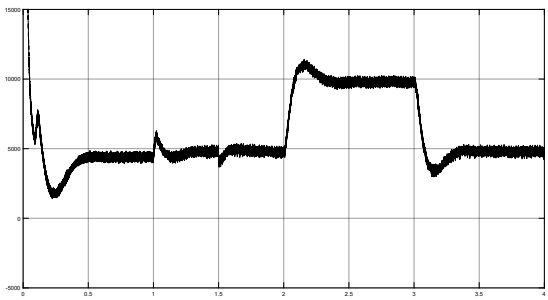

Figure 20. Wind turbines, photovoltaics, and energy storage pool power.

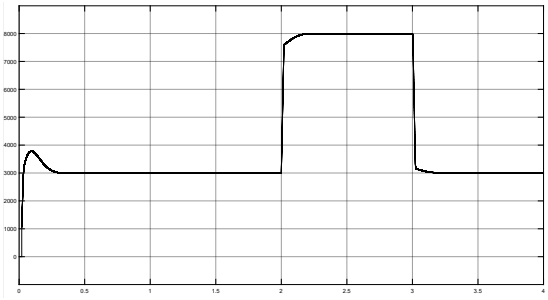

Figure 21. Load power.

Wind power generation, photovoltaic power generation, and energy storage system simulation results are shown in Figures 19–21. In the system, at t = 2 s, the load power suddenly changed from 3 kW to 8 kW, in t = 2 s and back to 3 kW, and from the simulation results it can be seen that when the load increases, wind turbines, photovoltaics, and energy storage convergence power can respond in time to make up for the lack of power, and in this process, the convergence voltage can remain constant, and wind power generation and photovoltaic power generation in high wind speed and high light intensity perform well, and can provide enough power to meet the load demand. The system responds quickly when the wind speed and light change, and can adjust the charge and discharge in time, and the energy storage system effectively balances the fluctuations of wind power and photovoltaic power generation, ensuring that the load has sufficient power supply at any time.

Based on the above simulation analysis, it is not difficult to find that this energy storage system can provide stable DC voltage support for the DC bus in different scenarios and has a relatively high-power output support. Therefore, it can be used as the DC input voltage of this DC/DC converter.

3. Topology and Model of the Hydrogen Production Power Supply Circuit

Electrolytic hydrogen production power sources play an important role in this. In this paper, a phase-shifted full-bridge modular DC high-current hydrogen production power supply design based on virtual impedance technology is proposed, which is converted to DC-DC through the phase-shifting full-bridge circuit, processed by the subsequent high-frequency transformer, and finally output to the load through the filter circuit. Virtual impedance technology is introduced into the control circuit to optimize the weight of the circuit and reduce the size of the current ripple.

The proposed hydrogen production power supply employs the topological structure illustrated in Figure 22, which consists of three key stages: a phase-shifted full-bridge DC-DC converter, a high-frequency isolation transformer, and an output filter circuit [17–24]. The phase-shifted full-bridge converter adjusts the input voltage, the high-frequency transformer provides electrical isolation and voltage scaling, and the filter circuit suppresses switching ripples before the power is delivered to the electrolyzer.

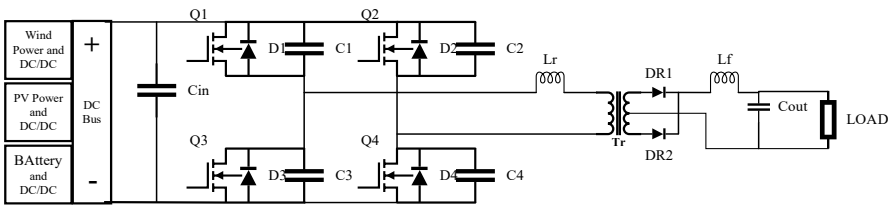

Figure 22. Main circuit topology.

To study the stability of the circuit and the subsequent addition of virtual impedance technology, it is necessary to model and analyze the DC-DC converter. Currently, the common method is to add the duty cycle part of the phase-shifted full-bridge loss under the buck circuit, and the linearization method is the average state method. The power supply section is composed of three parts, namely the wind power section, the photovoltaic section, the supercapacitor, and their DC/DC devices. Q1 and Q3 form the leading bridge arm, while Q2 and Q4 form the lagging bridge arm. D1–D4 are the reverse parallel diodes of the corresponding SiC MOSFETs, and C1–C4 are the corresponding diode parasitic capacitances. Lr is a resonant inductor in series on the primary side of the transformer, and Tr is a high-frequency transformer. The rectifier bridge is formed by DR1 and DR2, and the current is output to the load R after passing through the filter circuit. According to the state average method and small-signal analysis method, the model of a phase-shifting full-bridge circuit, as shown in Figure 23, can be obtained [25–29].

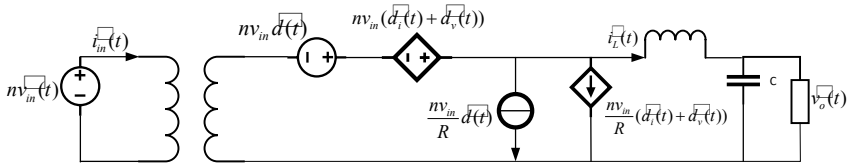

Figure 23. Phase-shifted full-bridge converter small-signal equivalent circuit.

Where $\hat{d}_i$ denotes the variation in duty cycle induced by changes in inductor current. $\hat{d}_v$ represents the variation in duty cycle caused by input voltage fluctuations, and $\hat{d}$ is the duty cycle variation on the transformer secondary side resulting from the primary side duty cycle adjustment. V_{in} is the input voltage; n is the transformer turn ratio coefficient.

Perform Thevenin equivalence on the left end of the circuit as shown in Figure 24.

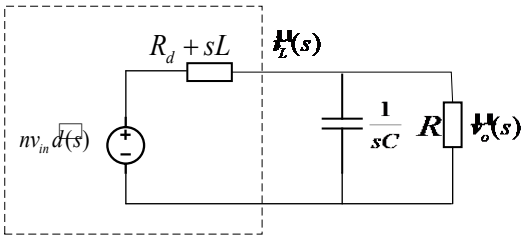

Figure 24. Thevenin equivalent circuit.

Where, in Figure 24: $R_d = 4n^2 L_r f_s$.

According to the above equivalent circuit, Equation (11) can be obtained.

$$\begin{cases} \hat{v}_o(s) = nV_{in}\hat{d}(s)\frac{R//\frac{1}{sC}}{R//\frac{1}{sC}+R_d+sL} \\ \hat{i}_L(s) = \frac{nV_{in}\hat{d}(s)}{R//\frac{1}{sC}+R_d+sL} \end{cases} \tag{11}$$

The transfer function Equation (12) is obtained from the above Equation (11).

$$G_{vd}(s) = \frac{\hat{v}_o(s)}{\hat{d}(s)} = \frac{nV_{in}}{LCs^2 + (R_dC + \frac{L}{R})s + \frac{R_d}{R} + 1} \tag{12}$$

$$G_{vd}(s) = \frac{\hat{i}_L(s)}{\hat{d}(s)} = \frac{nV_{in}(Cs + \frac{1}{R})}{LCs^2 + (R_dC + \frac{L}{R})s + \frac{R_d}{R} + 1} \tag{13}$$

$$G_{vi}(s) = \frac{\hat{v}_o(s)}{\hat{i}_L(s)} = \frac{R}{RCs + 1} \tag{14}$$

The control circuit is shown in Figure 25, which adopts PI double closed-loop control. The front end is the input end, which mainly includes the current setting and other parameters, and the end output is the shift Angle, to control the MOSFETs of the full bridge. To study the high current characteristics, this paper also designs (as shown in Figure 26) the case of two devices in parallel to form a high current, and based on this case, proposes the virtual impedance technology to optimize the current design.

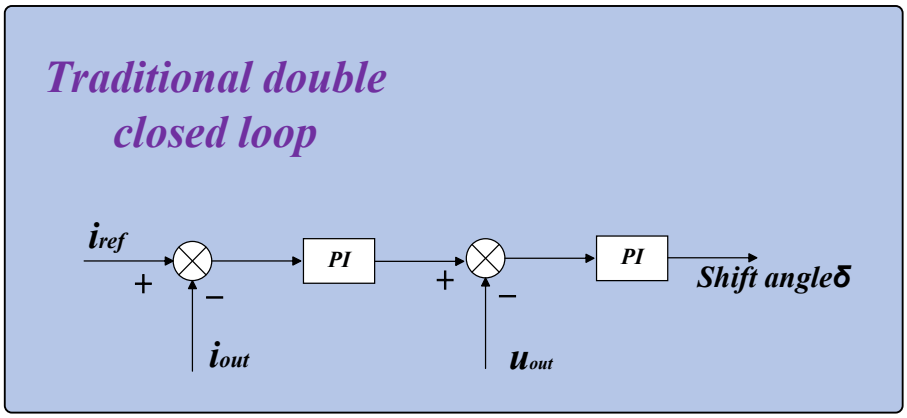

Figure 25. PI double closed-loop control block diagram.

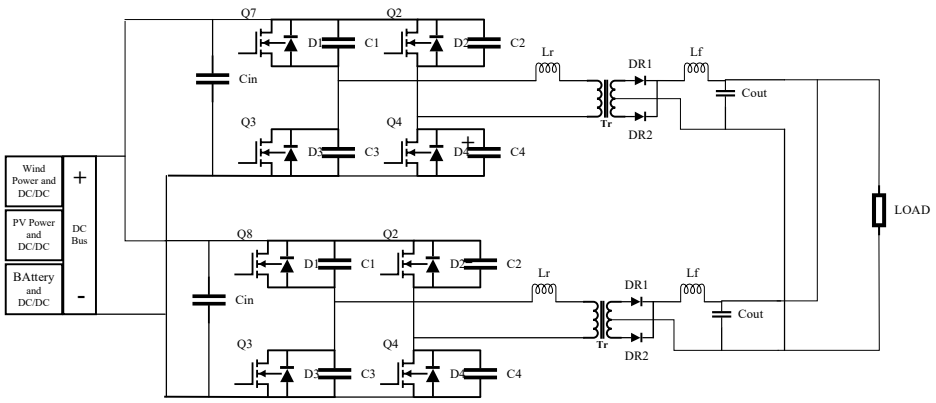

Figure 26. Parallel topology diagram of hydrogen production power supply modules.

4. Virtual Impedance Technology

To suppress the ripple size, the simplest solution is to increase the filter inductance. Because the target current of the large current generator is large, the inductor is huge, and the large inductor will inhibit the current rise rate, so it cannot meet the requirements of simulating the large rise rate of short circuit current. So, to avoid the above problems, virtual impedance technology can be used.

Virtual impedance is mainly used in the droop control of the AC power grid, and the purpose is to make the power grid appear purely inductive. However, in this design, the main work is to use the virtual inductor to increase the filtering effect and suppress the ripple. Compared to the traditional PI control, the control chart is shown in Figure 27.

Figure 27 shows that, on the basis of the traditional PI control, virtual impedance is introduced based on the inner loop, which mainly includes inductors and filters. The introduction of virtual impedance (virtual inductance *Lv*) is mathematically manifested as differentiating the current command *iref* output by the outer loop and multiplying it by the inductance parameters to simulate the voltage drop across the inductance.

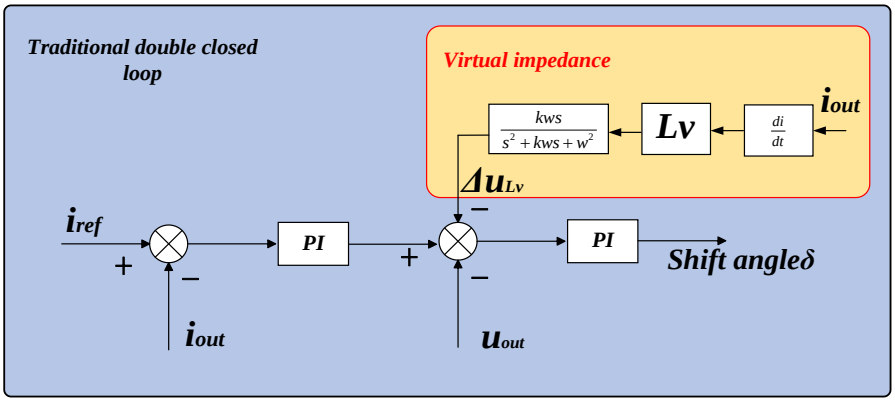

Figure 27. Virtual impedance control block diagram.

The generated V_{Lv} then passes through a bandpass filter, and the transfer function is

$$\frac{kws}{s^2 + kws + w^2} \tag{15}$$

The virtual impedance controller acts on the converter's output voltage/current, while the on/off actions of the power switches (IGBT, MOSFET) generate a periodic ripple whose fundamental frequency equals the switching frequency (e.g., 100 kHz). The band-pass filter must therefore be centered exactly on this fundamental: only when the center frequency coincides with the switching frequency can the filter capture the ripple with maximum gain, prevent leakage caused by any frequency offset, and leave all other useful components—such as dynamic response or low-frequency load disturbance signals unaffected [30–34]. This filter is used to precisely select the specific frequency ripple components that need to be suppressed (such as specific harmonics), where ω is usually the center frequency, taken as the switching frequency of 100 khz, the appropriate value of k is selected through calculation and simulation results to suppress the switching frequency ripple (100 kHz) and to ensure good damping characteristics, resulting in minimal oscillation during the regulation process, and the value of k is ultimately determined to be 0.76. The filtered signal Δu_{Lv} is used as the compensation quantity. This compensation signal is usually superimposed with the output voltage u_{out} reference signal to correct the final phase shift Angle δ, to achieve ripple suppression.

According to the ripple calculation Equation (15), where $V_{o(\min)}$ is the minimum value of secondary side voltage output, f_s refers to the switching tube frequency of 100 kHz, D refers to the effective duty cycle, V_{in} refers to the input voltage, k refers to the transformer ratio, V_{Lf} refers to the voltage drop on the inductor, which is 1 V, and V_D refers to the tube voltage drop of the diode, and is ignored in the following calculation [35–38].

$$\Delta I = \frac{V_{o(\min)}}{2f_s L_f}\left(1 - \frac{V_{o(\min)}}{\frac{DV_{in}}{k} - V_{L_f} - V_D}\right) \tag{16}$$

When the filter inductance is 0.65 μH, the theoretical value of the current ripple is calculated by Equation (16). To reduce the current ripple to about 1%, the inductance value required is calculated by Equation (17).

$$\Delta I = \frac{V_{o(\min)}}{2f_s L_f} \times \left(1 - \frac{V_{o(\min)}}{\frac{DV_{in}}{k} - V_{L_f} - V_D}\right) = 26\ \text{A} \tag{17}$$

$$L_f = \frac{V_{o(\min)}}{2f_s I_{o(\max)} \times 0.01} \times \left(1 - \frac{V_{o(\min)}}{\frac{DV_{in}}{k} - V_{L_f} - V_D}\right) = 0.73\ \mu\text{H} \tag{18}$$

In practice, it is often larger than this calculated value.

From a Bode plot point of view, the open-loop transfer function is calculated by Equation (18).

$$G_{id} = \frac{i}{d} = \frac{3.6e-6s+1.2e5}{3.35e-16s^2+4.5e-4.4s+6.78} \tag{19}$$

The corresponding Bode plot is shown in Figure 28. It can be concluded that the phase margin of this Bode diagram is approximately 40 degrees, and the system is in a stable state.

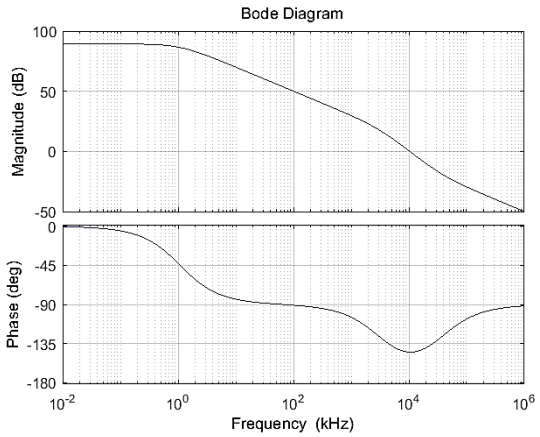

Figure 28. Open-loop control system Bode chart.

Figure 29 compares the Bode chart of the closed-loop control system under double PI control and double PI with virtual impedance control. The introduction of virtual inductors provides a constant +90° phase lead for the pure differential terms in the frequency domain, and the influence on the phase frequency at this point is very small. Therefore, it can be seen that the phase lead is nearly 90 degrees near the switching frequency of 100 khz, and the amplitude–frequency change is very small.

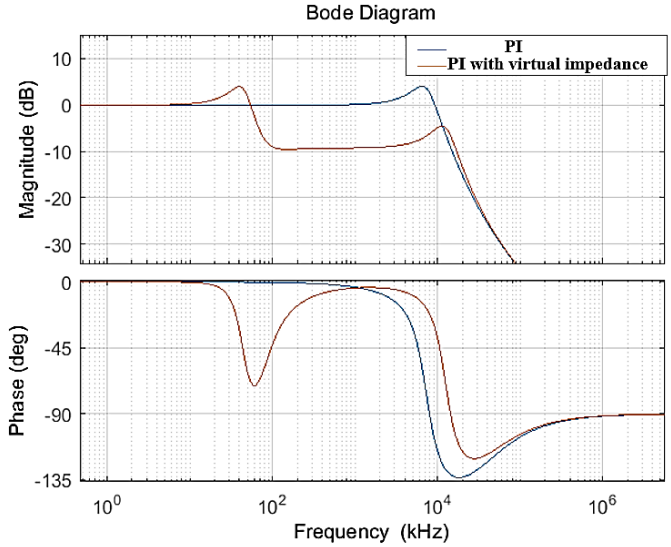

Figure 29. Closed-loop control system Bode chart with virtual impedance.

5. Simulation Analysis

This design relies on MATLAB/Simulink (R2021).

5.1. Simulation of Mixed Power Supply Voltage Input

The power supply section is a hybrid power supply composed of wind energy, photovoltaic power, and supercapacitors, which is required to provide a stable voltage input for the phase-shifted full bridge. The design is controlled by the PI to obtain an input voltage of 600 V, and the input waveform is shown in the following Figure 30. Sample the data from Figure 30 at a sampling interval of 0.01 s, and output it as a data file for the programmable power supply to simulate the output of the wind–solar–storage system.

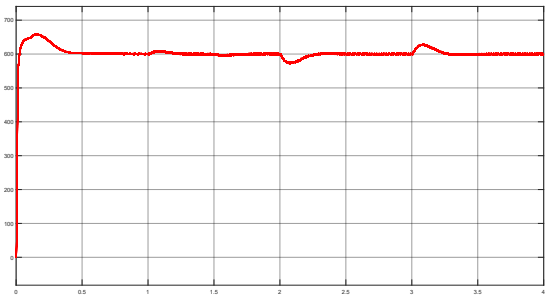

Figure 30. Mixed power supply output voltage.

5.2. Simulation of Rated Load Current

The design of the power supply mainly focuses on the control of the current ripple required by the output of the hydrogen production power supply under different load conditions. Firstly, the simulation of the constant load needs to simulate the normal current waveform to verify whether the normal current waveform can be normally generated, and the effect of the proposed virtual impedance technology on the ripple is compared. The simulation is set to a current of 600 A at the SiC MOSFETs switching frequency of 100 kHz, and the filter inductance is 0.5 μH.

Figure 31 shows the simulation results, and the above figure shows the current generated without adding virtual impedance. The ripple is about 36 A, and the proportion of ripple is 6%. The following figure shows the current generated without adding the virtual impedance, which is about 26.7 A, and the proportion of ripple is 4.45%. It can be seen that the virtual impedance can better suppress the ripple and make the output curve stable in a smaller range to provide more accurate data.

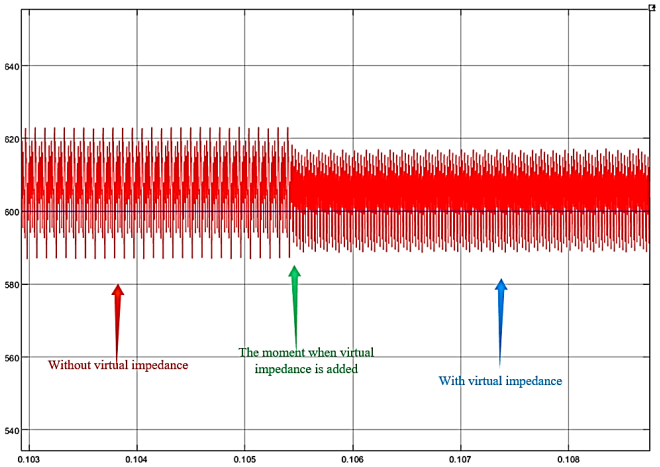

Figure 31. Virtual impedance control effect comparison under 600 A load current.

6. Experimental Result

In addition, according to the above simulation analysis, the parallel connection of multiple hydrogen production power sources is carried out to achieve greater capacity.

Figure 32 is the circuit diagram, which adopts the parallel input parallel output mode (IPOP) [39–43]. The capacity of power can be conveniently expanded. In Figure 32, a 600 V DC power supply is used, where L_r and C_r refer to the filter inductor and capacitor, and R is the output load.

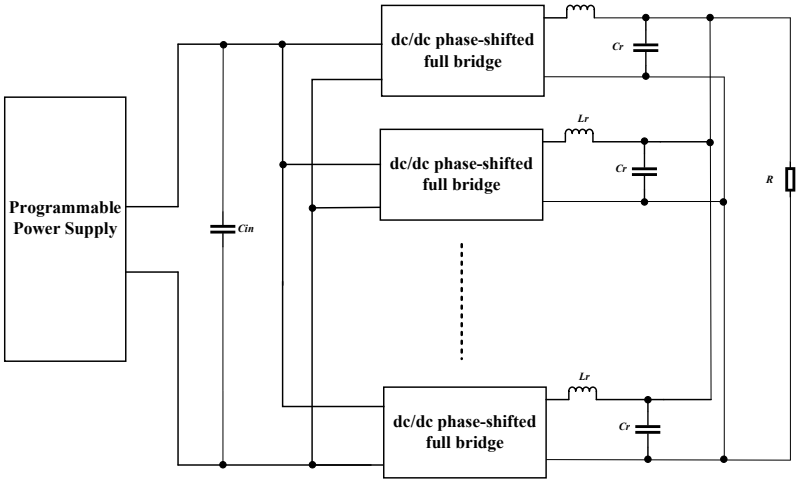

Figure 32. Power supply parallel topology diagram.

Figure 33 shows the experimental setup.



(**a**) (**b**)

Figure 33. Power supply, device for hydrogen production, and current waveform recording device. (**a**) Programmable power supply; (**b**) hydrogen power.

Figure 33 shows that the programmable power supply is used to simulate the output of wind, solar, and energy storage power sources. The hydrogen production power supply utilizes SiC MOSFETs (Infineon IMW120R014M1H (Infineon Technologies AG, Neubiberg, Germany)) as switching devices. A total output current of 5000 A is achieved by paralleling two identical power modules, with each module incorporating four SiC MOSFETs in a phase-shifted full-bridge configuration. Input and output voltage/current waveforms are recorded using a Keyvia KF1310 waveform acquisition device (Keyvia Electric, Tianjin, China), which offers a current measurement accuracy of 0.03% Full Scale and a voltage measurement accuracy of 0.02% Full Scale. The CHB-6KA (Beijing SENSOR Electronics, Beijing, China) is used to measure the current, which serves as feedback for the controller, and then the data is transmitted back to the host computer for waveform reconstruction. The output copper busbar is connected to a 1000 mm^2 high-current multi-strand copper braided wire, which is then connected to a shunt with a rating of 6 mV/1000 A. The shunt has a temperature coefficient less than 10 $ppm \cdot K^{-1}$. The total resistance of the

positive and negative busbars and the connecting copper cable was measured with a micro-ohmmeter to be approximately 6 μΩ. The Keyvia, KF1310 voltage channel has an accuracy of 0.02% Full Scale, and the current channel has an accuracy of 0.03% Full Scale. The system employs synchronous sampling at 10 kHz, using a 'high-frequency averaging + periodic integration' mode with a 100 ms window to eliminate 100 kHz switching ripple (the target frequency of the virtual impedance control). The shunt signal is connected to the analyzer via a 4-wire Kelvin connection. The analyzer automatically compensates for a line resistance of 0.5 mΩ. The analyzer synchronously records the input and output voltages and currents. The combined uncertainty of the main components, including the input, output, connecting cables, and terminal blocks, is estimated based on the Guide to the Expression of Uncertainty in Measurement (GUM, ISO/IEC GUIDE 98-3:2008) [44]. With an uncertainty budget factor kc = 2 and a 95% confidence level, the expanded uncertainty is calculated to be 0.66%. Based on the data recorded over 10 s, power changes are recorded and efficiency is analyzed, resulting in an efficiency of $\eta_{\min} = 95.7\%$. So, the efficiency at 5000 A can be calculated as $\eta \approx 95\%$.

The device outputs a load current of 5000 A, and the field experimental results are shown in Figure 34. It can be seen that the output of the device can reach 5000 A.

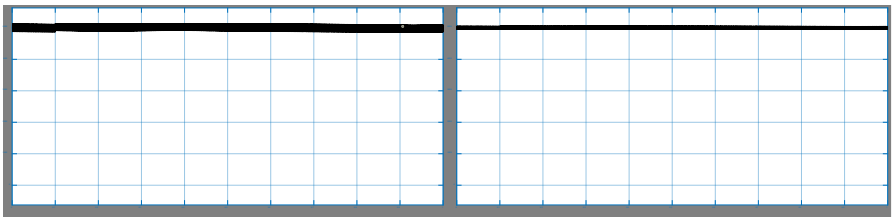

(**a**) (**b**)

Figure 34. Experimental results of virtual impedance control effect comparison under 5000 A load current (**a**) without virtual impedance and (**b**) with virtual impedance.

Figure 35 shows that when virtual impedance control is not added, the 5000 A load current can better reach the set value, but the current ripple is large, and the maximum is 177 A. After adding virtual impedance control, the ripple is reduced to about 106 A.

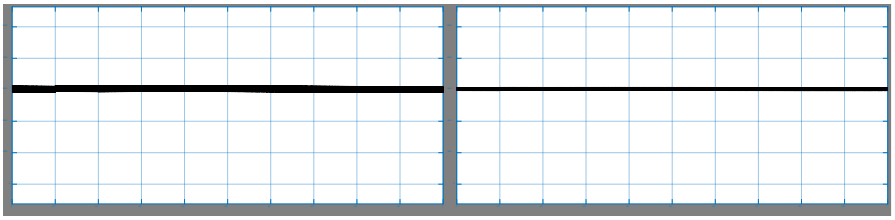

(**a**) (**b**)

Figure 35. Experimental results of virtual impedance control effect comparison under 3000 A load current (**a**) without virtual impedance and (**b**) with virtual impedance.

Figure 36 shows that when virtual impedance control is not added, the 3000 A load current can better reach the set value; the current ripple is larger than that after virtual impedance control is added, with a maximum of 91 A, and the ripple is reduced to about 44 A after virtual impedance control is added.

To evaluate the virtual impedance control dynamic performance, the load increasing and load fluctuation experiments were carried out, and the current waveform was recorded.

Figure 37 shows that when the load current increases from 1500 A to 1800 A, the current ripple is larger, with a maximum of 53 A when virtual impedance control is not

added, and the ripple is reduced to about 31 A after virtual impedance control is added. The current change can follow the load change well and quickly.

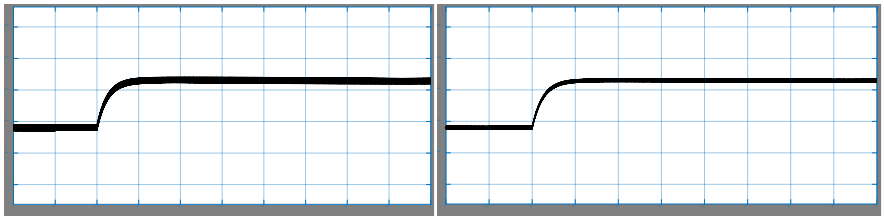

(**a**) (**b**)

Figure 36. Experimental results of virtual impedance control effect comparison when increasing load (**a**) without virtual impedance and (**b**) with virtual impedance.

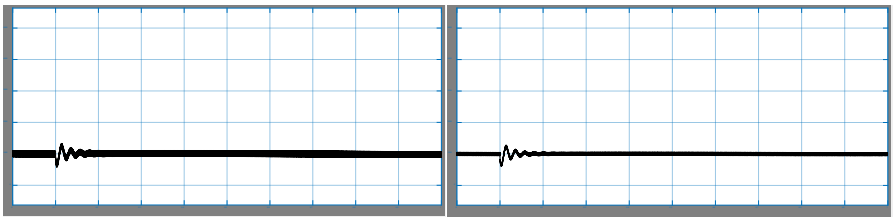

(**a**) (**b**)

Figure 37. Experimental results of virtual impedance control effect comparison when load fluctuations are (**a**) without virtual impedance and (**b**) with virtual impedance.

Figure 37 shows that when the output load current is 1000 A, the maximum fluctuation amplitude is about 400 A. When the virtual impedance control is not added, the current ripple is large, and the maximum is 26 A. After adding the virtual impedance control, the ripple is reduced to about 16 A.

As presented in Table 1, under all tested load current conditions, the virtual impedance control strategy achieves superior ripple suppression compared to the conventional PI control. Additionally, the power supply maintains high efficiency across the entire load range, with average efficiency values exceeding 95% (e.g., 95.2% at 5000 A, 96.2% at 3000 A), demonstrating the proposed strategy's ability to balance ripple reduction and efficiency.

Table 1. Output current and efficiency under different output current conditions.

Load Current Condition	Without Virtual Impedance		With Virtual Impedance		Average Efficiency with Virtual Impedance Control of Power η%
	Maximum Ripple Current Value $\Delta I_{PP(MAX)}$	Percentage of Current Ripple Value ΔI%	Maximum Ripple Current Value $\Delta I_{PP(MAX)}$	Percentage of Current Ripple Value ΔI%	
5000 A	177 A	3.54	106 A	2.10	95.2
3000 A	91 A	3.03	44 A	1.47	96.2
1500 A → 1800 A (load increase)	53 A	2.94	31 A	1.72	95.3
1000 A (fluctuation)	26	2.60	16 A	1.60	96.0

Virtual impedance significantly suppresses ripple in all load segments, and after enabling virtual impedance, both the maximum ripple current ΔIPP(MAX) and the ripple percentage ΔI% dropped significantly, as follows: 5 kA condition: the ripple percentage dropped from 3.54% to 2.10%, a reduction of about 40%; 3 kA condition: the ripple percentage dropped from 3.03% to 1.47%, a reduction of about 51%; and 1 kA fluctuating segment: the ripple percentage dropped from 2.60% to 1.60%, a reduction of about 38%. This indicates that virtual impedance control is effective for both high and low current segments, with the best effect near 3 kA.

Minimal and stable efficiency loss. After introducing virtual impedance, the average efficiency remains at 95.2–96.2%; the highest efficiency occurs at the 3 kA segment (96.2%), corresponding to the maximum ripple suppression. This shows that the proposed strategy improves current quality without significant additional loss.

Comprehensive benefits of virtual impedance control achieve an average reduction in ripple current by more than 40% at the cost of less than 0.3% efficiency, which is beneficial for reducing the size of filters, extending the life of capacitors, and meeting the low ripple demand of high-precision loads.

7. Conclusions

In this paper, a design of a phase-shift full-bridge modular DC high-current hydrogen production power supply based on virtual impedance technology for offshore wind–solar–storage–power hydrogen production power supply is proposed. Experimental results demonstrate that the virtual inductance control strategy reduces the maximum current ripple by 40% (from 3.54% to 2.10%) at 5 kA, 51% (from 3.03% to 1.47%) at 3 kA, and 38% (from 2.60% to 1.60%) at 1 kA. The additional power loss introduced by the control algorithm is less than 0.3%, while the average efficiency remains above 95.2% across the entire load range of 1–5 kA, the 40% ripple reduction allows a 30% smaller DC-link capacitor and lower inductance, saving total converter cost and extending capacitor lifetime, without any hardware change to the output filter. Overall, the proposed virtual impedance-based phase-shifted full-bridge modular power supply effectively suppresses current ripples, addresses the challenge of excessive ripple in high-current hydrogen production applications, and maintains rapid dynamic responses to load changes. It is well suited for various types of electrolyzers, offering both low output ripple and high efficiency. Future work will focus on optimizing the virtual impedance parameters for wider load ranges and verifying the system's long-term stability in actual offshore wind–solar–storage integrated systems.

Author Contributions: Conceptualization and funding acquisition, P.C.; writing—original draft, J.Z. and Q.F.; formal analysis and software, L.C.; writing—review and editing, C.W. and L.M. All authors have read and agreed to the published version of the manuscript.

Funding: This research is partly supported by the National Key R&D Program of China (grant number 2023YFB4005105).

Data Availability Statement: The original research results presented in this study have been included in the article. For further inquiries, please contact the corresponding author.

Conflicts of Interest: The authors declare no conflicts of interest.

References

1. Qin, F. Economic Analysis of Hydrogen Production from Electrolytic Water Considering Carbon Emissions. In Proceedings of the 2022 12th International Conference on Power and Energy Systems (ICPES), Guangzhou, China, 23–25 November 2022; pp. 1–5.
2. Ursua, A.; Gandia, L.M.; Sanchis, P. Hydrogen Production from Water Electrolysis: Current Status and Future Trends. *Proc. IEEE* **2012**, *100*, 410–426. [CrossRef]
3. Zhou, J.X.; Sun, L.Y.; Liu, T.Z.; Zhu, Y.Q. Exploration into the Influence of Uncertainty on the Suppression of Hydrogen Production Characteristics in New Energy Systems. In Proceedings of the 2024 4th International Conference on Energy Engineering and Power Systems (EEPS), Hangzhou, China, 9–11 August 2024; pp. 1–6.
4. Zhong, Y.J. Summary of Hydrogen Industry Development and Application Prospect: The Case of China. In Proceedings of the 2022 IEEE 5th International Electrical and Energy Conference (CIEEC), Nanjing, China, 27–29 May 2022; pp. 1–4.
5. Song, X.Y.; Liang, D.X.; Song, J.; Xu, G.Z.; Deng, Z.F.; Niu, M. Problems and Technology Development Trends of Hydrogen Production from Renewable Energy Power Electrolysis—A Review. In Proceedings of the 2021 IEEE 5th Conference on Energy Internet and Energy System Integration (EI2), Taiyuan, China, 22–24 October 2021; pp. 1–7.

6. Yu, H.M.; Shao, Z.G.; Hou, M.; Yi, B.L. Hydrogen Production by Water Electrolysis: Progress and Suggestions. *Chin. Eng. Sci.* **2021**, *23*, 146–152. [CrossRef]
7. Jiang, Z.Y.; Yin, J.Y.; Lu, T.G.; Sheng, L.; Zhao, P.; Li, W.T. Considering the New Energy Outgoing Multi-Energy Complementary System Architecture for the Local Utilization of Hydrogen Energy and Its Pre-Day Optimized Scheduling Strategy. In Proceedings of the 2024 3rd International Conference on Energy, Power and Electrical Technology (ICEPET), Chengdu, China, 17–19 May 2024; pp. 1–8.
8. Garrigos, A.; Blanes, J.M.; Carrasco, J.A. 5 kW DC/DC Converter for Hydrogen Generation from Photovoltaic Sources. *Int. J. Hydrogen Energy* **2010**, *35*, 6123–6130. [CrossRef]
9. Xin, C. Research on High Power Step-Down DC/DC Converter for Photovoltaic Hydrogen Production System. Master's Thesis, Hefei University of Technology, Hefei, China, 2021.
10. Concha, D.; Renaudineau, H.; Hernandez, M.S. Evaluation of DCX Converters for Off-Grid Photovoltaic-Based Green Hydrogen Production. *Int. J. Hydrogen Energy* **2021**, *46*, 19861–19870. [CrossRef]
11. Török, L.; Nielsen, C.K.; Munk-Nielsen, S.; Rømer, C.; Flindt, P. High Efficiency Electrolyser Power Supply for Household Hydrogen Production and Storage Systems. In Proceedings of the 2015 17th European Conference on Power Electronics and Applications (EPE'15 ECCE-Europe), Geneva, Switzerland, 8–10 September 2015; pp. 1–10.
12. Gautam, D.S.; Bhat, A.K.S. A Comparison of Soft-Switched DC-to-DC Converters for Electrolyzer Application. *IEEE Trans. Power Electron.* **2012**, *27*, 54–60. [CrossRef]
13. Wang, M.Y.; Niu, S.K.; Pang, X.Z.; Ren, Q.C.; Shen, Y.Q.; Chen, A.L. A Power Decoupling Control Strategy for Virtual Oscillator Controlled Grid-Forming Inverters Based on Impedance and Voltage Compensation. In Proceedings of the 2023 IEEE 2nd International Power Electronics and Application Symposium (PEAS), Guangzhou, China, 10–13 November 2023; pp. 1–6.
14. Hao, C.; Hengyu, L.; Xuchen, L.; Defu, W.; Tie, G.; Wei, W. Parallel Inverter Circulating Current Suppression Method Based on Adaptive Virtual Impedance. In Proceedings of the 2019 4th International Conference on Power and Renewable Energy (ICPRE), Chengdu, China, 21–23 September 2019; pp. 1–5.
15. Tang, J.L.; Soua, S.; Mares, C.; Gan, T.H. An Experimental Study of Acoustic Emission Methodology for In-Service Condition Monitoring of Wind Turbine Blades. *Renew. Energy* **2016**, *99*, 170–179. [CrossRef]
16. Omar, N.; Monem, M.A.; Firouz, Y.; Salminen, J.; Smekens, J.; Hegazy, O.; Gaulous, H.; Mulder, G.; Van den Bossche, P.; Coosemans, T.; et al. Lithium Iron Phosphate-Based Battery—Assessment of the Aging Parameters and Development of a Cycle Life Model. *Appl. Energy* **2014**, *113*, 1575–1585. [CrossRef]
17. Dahal, M.; Krishan, R. Distributed Adaptive Virtual Impedance Control for Power Sharing in an Islanded Microgrid. In Proceedings of the 2024 Second International Conference on Smart Technologies for Power and Renewable Energy (SPECon), Ernakulam, India, 2–4 April 2024; pp. 1–7.
18. Fan, B. A Novel Droop Control Strategy of Reactive Power Sharing Based on Adaptive Virtual Impedance in Microgrids. *IEEE Trans. Ind. Electron.* **2022**, *69*, 11335–11347. [CrossRef]
19. Li, Y.T.; Gu, Y.J.; Zhu, Y.; Junyent-Ferré, A.; Xiang, X.; Green, T.C. Impedance Circuit Model of Grid-Forming Inverter: Visualizing Control Algorithms as Circuit Elements. *IEEE Trans. Power Electron.* **2021**, *36*, 3377–3395. [CrossRef]
20. Yang, L.S.; Lin, C.C. Analysis and Implementation of a DC-DC Converter for Hybrid Power Supply Systems. *J. Power Electron.* **2015**, *15*, 1438–1445. [CrossRef]
21. Kim, D.H.; Kim, H.W.; Park, J.H.; Jeon, H.J. High Efficiency High-Step-Up Single-Ended DC-DC Converter with Small Output Voltage Ripple. *J. Power Electron.* **2015**, *15*, 1468–1479. [CrossRef]
22. Petreus, D.; Ionut, C.; Patarau, T.; Etz, R.; Orban, Z. The Effect of Parasitic Capacitances on the Phase-Shift Full Bridge Converter. In Proceedings of the IECON 2019-45th Annual Conference of the IEEE Industrial Electronics Society, Lisbon, Portugal, 14–17 October 2019; pp. 1–6.
23. Zhang, X.J.; Li, C.Y.; Yang, H.; Guan, Y.S. Control Strategy Analysis and Loop Design of Full-Bridge Phase-Shift Soft-Switching DC-DC Converter. In Proceedings of the 2016 IEEE 8th International Power Electronics and Motion Control Conference (IPEMC-ECCE Asia), Hefei, China, 22–26 May 2016; pp. 1–5.
24. Zhao, L.; Li, H.Y.; Yu, Y.X.; Wang, Y.T. A Novel Method of Phase-Shifted Full-Bridge Converter to Improve Efficiency Under Light Load Conditions. In Proceedings of the 2015 9th International Conference on Power Electronics and ECCE Asia (ICPE-ECCE Asia), Seoul, Republic of Korea, 1–5 June 2015; pp. 1–6.
25. Xiao, J.J.; Wang, L.; Qin, Z.A.; Bauer, P. An Adaptive Virtual Impedance Control for Reactive Power Sharing in Microgrids. In Proceedings of the 2023 IEEE Energy Conversion Congress and Exposition (ECCE), Nashville, TN, USA, 29 October–2 November 2023; pp. 1–6.
26. Weng, Z.Y.; Cheng, Y.; Cheng, Y.; Weng, Z.G.; Ge, G.; Fang, J. Steady State Analysis and Simulation of Phase-Shifting Full Bridge Series Resonant Converter. In Proceedings of the 2024 7th Asia Conference on Energy and Electrical Engineering (ACEEE), Chengdu, China, 20–22 July 2024; pp. 1–8.

27. Wang, S.S.; Shi, Z.H.; Ruan, J.H. Small-Signal Modeling of Phase-Shift Full-Bridge Converter with Peak Current Mode Control. In Proceedings of the 2020 IEEE International Conference on Applied Superconductivity and Electromagnetic Devices (ASEMD), Tianjin, China, 16–18 October 2020; pp. 1–4.
28. Sun, X.D.; Zhou, Y.H.; Chen, G.T.; Ren, B.Y. Model Predictive Control of a Phase-Shifted Full-Bridge DC-DC Converter. In Proceedings of the 2020 IEEE 9th International Power Electronics and Motion Control Conference (IPEMC2020-ECCE Asia), Nanjing, China, 29 November–2 December 2020; pp. 1–5.
29. Bhargavi, P.; Chaganti, P.C.V.; Sowmya, V.; Manitha, P.V.; Lekshmi, S. A Comparative Study of Phase-Shifted Full Bridge and High-Frequency Resonant Transistor DC-DC Converters for EV Charging Application. In Proceedings of the 2022 IEEE 2nd International Conference on Mobile Networks and Wireless Communications (ICMNWC), Tumkur, Karnataka, India, 2–3 December 2022; pp. 1–6.
30. Wu, H.B.; Li, Q.; Sun, Z.J.; Li, C.; Liu, Y.Z.; Chen, X.S. Modeling and Simulation of Fractional-Order Phase-Shifted Full-Bridge Converters. In Proceedings of the 2023 5th International Conference on Power and Energy Technology (ICPET), Tianjin, China, 27–30 July 2023; pp. 1–7.
31. Liu, H.M.; Zhao, Y.L.; Al Shurafa, M.; Chen, J.F.; Wu, J.; Cheng, Y.M. A Novel PID Control Strategy Based on PSO-BP Neural Network for Phase-Shifted Full-Bridge Current-Doubler Synchronous Rectifying Converter. In Proceedings of the 2021 IEEE 4th Advanced Information Management, Communicates, Electronic and Automation Control Conference (IMCEC), Chongqing, China, 18–20 June 2021; pp. 1–5.
32. Yu, H.; Shi, Y.; Wu, C.H.; Wang, F.; Xu, C. Input Series Output Parallel Phase-Shifted Full-Bridge Converter Design for Full Range Soft-Switching Effect and Minimum Output Current Ripple. In Proceedings of the 2023 IEEE PELS Students and Young Professionals Symposium (SYPS), Shanghai, China, 27–29 August 2023; pp. 1–6.
33. Liu, F.; Zhou, G.J.; Ruan, X.B.; Ji, S.Y.; Zhao, Q.L.; Zhang, X.Y. An Input-Series-Output-Parallel Converter System Exhibiting Natural Input-Voltage Sharing and Output-Current Sharing. *IEEE Trans. Ind. Electron.* **2021**, *68*, 1166–1177. [CrossRef]
34. Wang, Y.; Guan, Y.P.; Fosso, O.; Molinas, M.; Chen, S.Z.; Zhang, Y. An Input-Voltage-Sharing Control Strategy of Input-Series-Output-Parallel Isolated Bidirectional DC/DC Converter for DC Distribution Network. *IEEE Trans. Power Electron.* **2022**, *37*, 1592–1604. [CrossRef]
35. Mo, T.Z.; Li, N.; Zhang, Z.; Li, J.H.; Zhang, Z.H.; Pan, J.F. A Droop Control Method Based on Adaptive Virtual Impedance for Parallel Control of Distributed Generators. In Proceedings of the 2024 10th International Conference on Power Electronics Systems and Applications (PESA), Hong Kong, China, 5–7 June 2024; pp. 1–7.
36. Keddar, M.; Doumbia, M.L.; Belmokhtar, K.; Krachai, M.D. Experimental Validation of an Accurate Reactive Power-Sharing Approach Based on Adaptive Virtual Impedance and Consensus Control. In Proceedings of the 2021 12th International Renewable Energy Congress (IREC), Hammamet, Tunisia, 26–28 October 2021; pp. 1–6.
37. Liang, X.D.; Andalib-Bin-Karim, C.; Li, W.X.; Mitolo, M.; Shabbir, M.N.S.K. Adaptive Virtual Impedance-Based Reactive Power Sharing in Virtual Synchronous Generator Controlled Microgrids. *IEEE Trans. Ind. Appl.* **2021**, *57*, 46–60. [CrossRef]
38. Nie, B.; Li, X.M. A Control Method for Parallel Inverter with Adaptive Virtual Impedance. In Proceedings of the 2018 5th International Conference on Systems and Informatics (ICSAI), Nanjing, China, 10–12 November 2018; pp. 1–5.
39. Gurumurthy, S.K.; Cupelli, M.; Monti, A. A Generalized Framework for Synthesizing Virtual Output Impedance Control of Grid Integrated Power Electronic Converters. In Proceedings of the 2018 IEEE International Conference on Power Electronics, Drives and Energy Systems (PEDES), Chennai, India, 18–21 December 2018; pp. 1–6.
40. Moutevelis, D.; Roldán-Pérez, J.; Prodanovic, M.; Milano, F. Design of Virtual Impedance Control Loop Using the Complex Frequency Approach. In Proceedings of the 2023 IEEE Belgrade PowerTech, Belgrade, Serbia, 25–29 June 2023; pp. 1–6.
41. Roja, P.; John, V. Reexamining Phase-Shifted Full-Bridge Converter with PWM Ripple Current. In Proceedings of the 2021 National Power Electronics Conference (NPEC), Bhubaneswar, India, 15–17 December 2021; pp. 1–5.
42. Shahabi, A.; Lemmon, A.N. Modeling of ZVS Transitions for Efficiency Optimization of the Phase-Shifted Full-Bridge Topology. *IEEE J. Emerg. Sel. Top. Power Electron.* **2020**, *8*, 529–544. [CrossRef]
43. Mahapatra, M.; Pal, A.; Basu, K. Analysis and Design of Active Snubber of A Step-Up Phase Shifted Full Bridge DC-DC Converter Considering Parasitics. In Proceedings of the 2020 IEEE Energy Conversion Congress and Exposition (ECCE), Detroit, MI, USA, 11–15 October 2020; pp. 1–8.
44. *ISO/IEC GUIDE 98-3:2008*; Guide to the Expression of Uncertainty in Measurement (GUM). International Organization for Standardization: Geneva, Switzerland, 2008.

Disclaimer/Publisher's Note: The statements, opinions and data contained in all publications are solely those of the individual author(s) and contributor(s) and not of MDPI and/or the editor(s). MDPI and/or the editor(s) disclaim responsibility for any injury to people or property resulting from any ideas, methods, instructions or products referred to in the content.